Analysing expansional motion of Coronal Mass Ejections

Rishabh Verma

Thesis
Submitted Towards Partial Fulfillment
of
BS MS Dual Degree Program

Under the guidance of

Dr. P. Subramanian
Assistant Professor
Indian Institute of Science Education and Research
Pune, India

Department of Physical Sciences
Indian Institute of Science Education and Research Pune

April 2011

Certificate

This is to certify that this dissertation entitled "Analysing expansional motional of Coronal Mass Ejections" submitted towards the partial fulfillment of the BS MS Dual Degree Program at the Indian Institute of Science Education and Research, Pune, represents original research carried out by Rishabh Verma at the Department of Physical Sciences, Indian Institute of Science Education and Research Pune under the supervision of Dr. P. Subramanian during the academic year 2010-2011.

Rishabh Verma

Supervisor

Date:
Place:

Head, Physical Sciences

Date:
Place:

Acknowledgments

This work would not have seen the light of day, had it not been for the support of so many people.
I would like to take this opportunity to thank Dr. Prasad Subramanian, for being so patient with me. I was going through a rough patch in life for the past one and a half years. In that time, he supported me and constantly motivated me, to learn and strive to reach my goals. His expertise in the field of Solar Physics was the foundation around which I have built my work.

I would also like to express my gratitude towards Arub Babu K.P., without whose help, I would not have been able to even start this project. His brilliant ideas always came to my rescue, and his presence has been a calming effect on me, knowing that with him around, there would always be a solution for any problem I encountered.
Adwiteey Maurya has done the major portions of the surface area calculations mentioned in the appendix section. I just helped him tweek his idea. He was also gracious enough to let me introduce our work in my thesis.
I would like to thank the faculty and staff of IISER, Pune for being so supportive throughout my stay at IISER, Pune.
Over the last year, me and my batchmates at HR-1 have found a new member of this hostel, Fish, our dog. Fish constantly kept me in good mood, whenever I felt low.
I would like to thank my friends at IISER, Pune, especially the first batch of students, for just being themselves and for enjoying each and every moment to its extreme. I would especially like to thank Bedartha, for coming up with this template, which did make my life a lot easier.

None of this would not have been possible had it not been for my family. Mom and Dad, you all have been my biggest support. I thank God Almighty for all his blessings.

Abstract

The main aim of this project is to study the expansion of Coronal Mass Ejections (CMEs) from the Sun due to Lorentz self-forces. We use data from the SOHO/LASCO and STEREO/SECCHI coronographs. We assume a flux rope geometry for the CMEs and fit a polynomial to the data of flux rope minor radius vs time. We derive the expansional acceleration of the flux rope using the second derivative of this polynomial. In trying to examine if Lorentz self-forces are (primarily) responsible for flux rope expansion, we compute the predicted flux rope expansion rate using two prescriptions: 1) One in which the axial current enclosed by the nearly force-free flux rope configuration remains constant, and 2) one in which the axial current decreases approximately in inverse proportion to the height of the fluxrope from the Sun-center. The latter prescription is motivated by considerations of magnetic helicity conservation. We generally find that a model where the axial current decreases as $R^{-0.91}$ (where R is the heliocentric height of the flux rope CME) agrees best with the data.

Furthermore, we have computed the surface area of CMEs observed with SECCHI using a three-dimensional flux rope model. The variation of the flux rope surface area with time is expected to be a valuable tool in analyzing the drag force on a CME as it travels through the solar wind.

Contents

1 Introduction **1**
1.1 Coronal Mass Ejections 2
1.1.1 Causes: 3

2 Theory **5**
2.1 Studying the evolution of the minor radius of the CME 8

3 Methods **11**
3.1 Analysis done on LASCO data 11
3.1.1 For constant current: 12
3.1.2 For variable current: 13
3.2 Analysis done on SECCHI data 13
3.2.1 For variable current: 14

4 Results **15**
4.1 Analysis done on LASCO data 15
4.1.1 Analysis done on LASCO data, by assuming constant current. 16
4.1.2 Analysis done on LASCO data, by assuming variable current. 16
4.2 Analysis done on SECCHI data 18
4.2.1 Analysis for the variable axial current 18

5 Discussion **31**
5.1 For LASCO data 31
5.2 For SECCHI data 31

References **33**

Appendices **35**

Appendix A Surface Area Calculations **35**

Appendix B Results obtained from the surface area calculations **37**

Chapter 1

Introduction

The optical radiation that we see, is emitted from the photosphere (surface of the sun). These emissions are produced by Thompson scattering in the much more tenous atmosphere or the corona above, is many orders of magnitude less intense and hence can only be seen when the solar surface is occulted (e.g., by the moon during solar eclipses).

The observations of the solar corona date back to as early as 2800 B.C. Regular observations of solar eclipses and prominence started with the eclipse of 1842 A.D., which was observed by experienced astronomers like Airy, Arago, Baily, Littrow and, Struve. Photographic records started since 1851 eclipse in Norway and Sweden, when the professional photographer Berwoski succeeded to produce a daggueroty pe of prominence and the inner corona.
Bernard Lyot built the first coronagraph at Pic-du-Midi Observatory in 1930, an instrument that occults the bright solar disk and thus allows for routine coronal observations, without the need to wait for rare total eclipse events. In 1942, Edlén, identified the forbidden lines of highly ionized atoms and in this way established for the first time the million-degrees temperature of the corona.

The solar corona is divided into three major zones namely: (1) active regions (2) quiet sun regions and the (3) coronal holes.
Active Regions: The active regions on the solar surface are the areas where most the activity happens, but it actually makes up of a very small fraction of the total surface area. Active regions are located in areas of strong magnetic field concentrations, visible as sunspot groups in optical wavelengths or magnetograms. These groups typically exhibit a strong concentrated leading magnetic polarity, followed by a more fragmented trailing group of opposite polarity. Due to such bipolar nature, these regions are associated with closed magnetic field lines.
Quiet Regions: Because of recent technological advances this term has now become a misnomer, and is now classified in relative terms as an area where dynamic small scale phenomena like such as network heating events, nanoflares, explosive events, bright points, and soft X-ray jets, to large-scale structures that overarch quiet sun-regions are rooted in the active regions.
Coronal Holes: The northern and southern regions have been found to be darker

than the equatorial regions on the coronal surface. These are regions of open field lines that act as efficient conduits for flushing heated plasma from the corona into the solar wind. Because of this efficient transport mechanism, coronal holes are empty of plasma most of the times, and thus appear darker than the quiet sun.

The solar corona is observed during total eclipses or with an instrument called a coronagraph. Eclipses only occur roughly once a year while coronagraphs can record images of the solar corona all year long. Space coronagraphs like LASCO aboard the SOHO spacecraft and SECCHI aboard STEREO spacecraft, are positioned between the Sun and Earth, so that it can record images of the corona without interruptions of the night and day cycle we have on earth.

The software used on these satellites are intended to simulate the Thomson scattering of the photospheric light by the electrons of the corona. This is the component of the solar corona is called the K corona. This is in this component that we observe the most structured and transient phenomenons, like streamers and Coronal Mass Ejections (CMEs). The K corona is optically thin: the line of sight (LOS) are then simple straight lines.

The K corona structures that are observed, are linked to the solar magnetic field. Loops and streamers are the main structures we observe. They are related respectively to closed and open field lines.

The reversal of the magnetic polarity of the global solar magnetic field, modulates the total radiation output in many wavelengths in a dramatic way. This solar magnetic cycle is of about 11 years. The full cycle is of 22 years, after which the original magnetic configuration is restored, is called a *Hale cycle*. The total magnetic flux reaches a maximum during the peaks of the cycle and drops to a low level during the minimum of the cycle.
Since many radiation mechanisms are governed by dissipation of the magnetic energy and the resultant plasma heating, the radiation output in these wavelengths is correspondingly modulated from solar maximum to minimum. During a cycle, the active regions migrate from higher latitude to lower latitude near the equatorial region, leading to the butterfly diagram of the sunspots (Spörer's Law), when their latitudinal position is plotted with time.

1.1 Coronal Mass Ejections

Every main sequence star is losing mass, caused by the dynamic phenomena in the atmosphere that accelerate plasma or particles beyond the escape speed. The mass loss is accounted to broadly two main phenomena: the steady solar wind outflow and the sporadic ejection of the plasma structures (Coronal Mass Ejections). The frequency of such a phenomena is about a few per day, carrying mass in the range from $10^{14} - 10^{16}$g. The geometric shapes of such events have, range from fluxropes, semi-shells, or bubbles. Coronal Mass Ejection (CMEs) are dynamically evolving plasma structures, propagating outward from the sun into the inter-planetary space, carrying a frozen-in magnetic field and expanding in size. If a CME travels radially towards the earth, it is called halo-CME.

Some of them can travel toward Earth and can generate magnetic and particle storms. The main manifestation we can see on Earth are the aurora borealis. They can also have more dramatic consequences as they can damage orbiting satellites or irradiate astronauts. Understanding their mechanism is then of a particular interest for both science and space weather forecasts. The resultant geomagnetic storms in the Earth's Magnetosphere can cause disruption of global communications and navigation networks, or failure of satellites and commercial power systems.

The study of Coronal Mass Ejections (CMEs) started in the early 1970s and have been subject to intensive investigation. In coronagraph images, a CME is identified by a discrete electron density enhancement expanding outward from the sun. Such structures have spatial structures of the order of the solar radius (R0) near the sun and masses of $10^{14} - 10^{16}$g.
Although CMEs observed in coronagraphs have velocities biased towards the plane of the sky, there is a strong correlation between CMEs and large geomagnetic storms. White-light coronagraphs regularly record expulsions of plasma in the solar corona. The shape and sizes of coronal mass ejections (CMEs) vary from event to event.

1.1.1 Causes:

Various explanations have come to light, that give us an insight on the causes of CMEs based in terms of mechanical analogues: [1]
Thermal Blast Model: This model suggests that the driving force of the CME is caused by greatly enhanced thermal pressure, produced by a flare, which cannot be contained by a magnetic field and thus pushes CME outwards into the heliosphere. With recent investigation it was found that sometimes CME were launched first, and a flare-emitted emission later, or the relative timing of the two events was very close, hence this model has run out of favor.
Dynamo Model: This model suggests that there is a rapid generation of magnetic flux by real-time stressing of the magnetic field. The driver of the magnetic stressing is accomplished by rapid displacements of footpoints of a coronal magnetic field systems. Blackman & Brandenberg also suggest that the launch of a CME balances the conservation of magnetic helicity during the solar cycle, by simultaneously liberating small-scale twist and large-scale writhe of opposite sign.
Mass Loading Model: This models comes under the broad classification of *storage* and *release* models, which entails a slow build-up of magnetic stress before eruption begins. The mass loading process can be manifested in the form of a growing quiescent or eruptive filament. Theoretical studies compare the total magnetic energy in the pre-eruption and posteruption equilibrium configurations in order to demonstrate the plausible transitions from a higher to lower energy state.
Tether Release Model: Magnetically dominated configurations like coronal loops generally involve a balance between upward-directed magnetic pressure, and downward-directed force of magnetic tension. The field lines that hold the tension are called *tethers*. Once the tethers are released one after the other, the tension on the other tethers increases, until the strain becomes eventually large that the remaining tethers begin to break and the spring uncoils in a catastrophic explosion.

Tether Straining Model: This model is similar to the *tether release model*, except that the strain on the tethers is constant, but is distributed to fewer and fewer tethers with time until they break.

This chapter has been inspired by the book "Physics of the Solar Coronal" [2]

Chapter 2

Theory

The magnetic geometry of the Coronal Mass Ejections are of fundamental importance in understanding the dynamics of CMEs because the Lorentz force acting on the structure critically depends on the 3D configuration of the electric current (**J**) and magnetic field (**B**). Although magnetic field in the corona is not directly measurable, there are observable signatures in the CME dynamics that are characteristic of the flux-rope geometry [3]. There is a broad understanding, that CMEs are envisaged as a magnetic fluxrope, wound radially along the axis of the major radius R.
Figure 2.1 shows a schematic drawing of a magnetic flux rope. The electric current is localized to a current channel of major radius R and minor radius a, with components J_t and J_p in the toroidal and poloidal directions [4]. The magnetic field of the flux rope, given by

$$\mathbf{J} = (c/4\pi) \bigtriangledown \times \mathbf{B} \tag{2.1}$$

which the has poloidal component B_p and toroidal component B_t. The toroidal field is confined to the current channel, but the poloidal field can extend beyond. A helical field line inside the current channel and some poloidal field lines outside the current channel are also mentioned in the diagram. Coronal magnetic field B_c due to currents unrelated to the electric current is shown in the poloidal direction. By a flux rope, we refer to the current and the magnetic field of the system, including the poloidal field B_p outside the current channel (but not B_c).

The outward force per unit length f on the flux rope (in cgs units) is given by

$$f = \frac{I_0^2}{c^2 a}\Big[ln(\frac{8a}{r_0}) + \frac{l_i}{2} - \frac{3}{2}\Big] + \pi r_0^2(\nabla P_\infty) + I \times B_\infty - \pi\rho r_0^2 \frac{GM_\odot}{a^2} \tag{2.2}$$

[5] which is quite similar to the equation presented in [6] Yeh (1995), it also includes the Lorentz self-force, which was previously not in corporated in Yeh's (1995) treatment.
The defination of the magnetic field inside a magnetic field structure can be described with the use of the Lundquist solution [7] [8] in which the terms $(J \times B)$ vanish. But actually, in reality the Lorentz self-force do not actually vanish.
Upon looking at the Lundquist solution we find that it was derived with the assumption that current density was parallel to the magnetic field ($j = \alpha B$), which

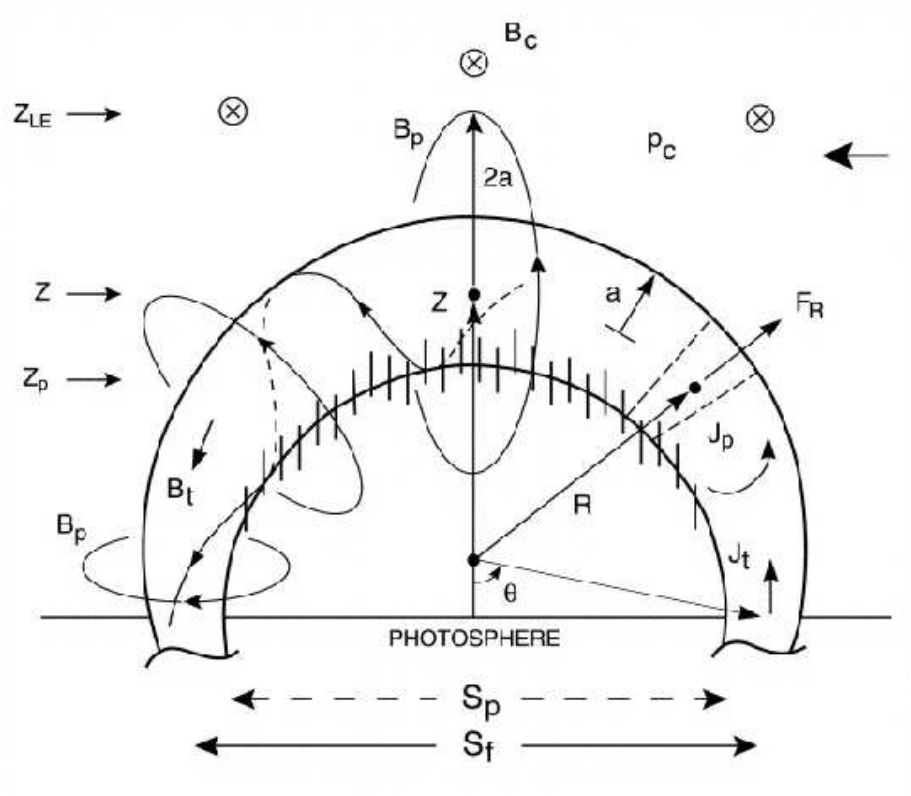

Figure 2.1: The figure from [3]. Schematic of a flux rope above the photosphere. The toroidal loop structure is the current channel with major radius R and minor radius a. The toroidal J_t and poloidal J_p currents and the corresponding poloidal B_p and toroidal B_t magnetic field components are indicated. Coronal pressure p_c and the overlying coronal field B_c (in the toroidal direction) are indicated. The outermost flux surface, represented by three poloidal field lines, is at $r = 2a(\theta)$ from the toroidal axis of the current channel, where $a(\theta)$ is the local minor radius at angular position . The centroid of the apex of the flux rope is at height Z from the base of the corona. The CME LE is at height $Z_LE = Z + 2a_a$ at the apex. The apex of the prominence is at $Z_p = Z - a_a$. These heights are indicated by the arrows on the left. The flux-rope footpoints are separated by S_f, measured center to center. The prominence footpoints are separated by $Sp = S_f - 2a_f$.

in turn implies the vanishing of the Lorentz stress [4]. The Lunquist solution would still remain valid in the regime where the current density and the magnetic field vectors make a very small angle κ with respect to each other. As $I_z \times B_\phi$ gives rise to the Lorentz self-force in the $\hat{r}$ direction (in cylindrical coordinates), leading to the expansion of the minor radius. Due the small misalignment in I_z (in the axial direction) gives rise to the translational motion. In the case of solar filaments, [9] Kumar and Rust (1994) showed that κ lying between 0.36° and 3.6° degrees is enough to support the dense filament material against solar gravity. Therefore, in this regime the Lundquist solution remains approximately valid even in the non-force-free cases. So in the case of a large aspect-ratio fluxrope, even a minute angle between the current density and magnetic field is sufficient to provide the required Lorentz force for the translational motion.

In Demoulin and Dasso 2009 [10], it is stated that the rapid decrease in total solar wind with the solar distance is the main factor which drives the expansion of the fluxrope. Factors such as internal over-pressure, the radial distribution and the amount of twists in the fluxrope have a minuscule effect on the expansion of the fluxrope.
In Wang et al. 2009 [11], it is stated that the both the thermal pressure force and the Lorentz self-force decrease rapidly as the CME moves out and the thermal pressure is the internal driver of the CME expansion.

In this study it is assumed that, the minor radius does not seem to affected by conditions in the external environment. The factor on which the evolution of the minor radius depends are mainly the conditions in the internal magnetic configration [4]. The major factors being the conservation of magnetic helicity and the axial flux. Hence, if the major radius of the fluxrope configuration of the CME increases (resulting in the increase in the length of the fluxrope), so as to ensure the conservation of magnetic helicity and the axial flux, an expansion in the fluxrope, implying that the minor radius of the CME increases. Further observations also show that the evolution of the minor and the major radius of the CME moving in the inter-planetary space evolve linearly with time.
The energy of a current ring (the cross-section of the CME) is given by

$$W = LI^2/2 \;\approx\; I^2 R[ln(8R/a) - 7/4] \tag{2.3}$$

[12] where I, R, a, and L are the current, major and minor radius, and the inductance of the ring, respectively. Since magnetic energy must be released in order to accelerate the ejecta (CMEs) and the term in brackets ($[ln(8R/a) - 7/4]$) does not vary strongly, the current in the rising flux loop of the CME must decrease faster than $R^{-\frac{1}{2}}$. In the approximation the current in the loop decreases roughly as R^{-1}, because the number of field line turns in the loop is conserved. Consequently, only a minor part of the initial relative helicity leaves the system with the ejected flux. We will see that the data do indeed conform to the law $I \propto R^{-0.91}$.

2.1 Studying the evolution of the minor radius of the CME

In order to facilitate the study of hydrodynamic properties of the CMEs, a circular cross-section of the magnetic cloud (CME) is considered [6]. This section is assumed to be moving in the heliographic equitorial plane, with axis oriented perpendicular to the plane. The heliocentric distance and azimuth of the cloud's axis, is denoted by r_0 and θ_0 in the polar coordinates (r, θ), which change with time.

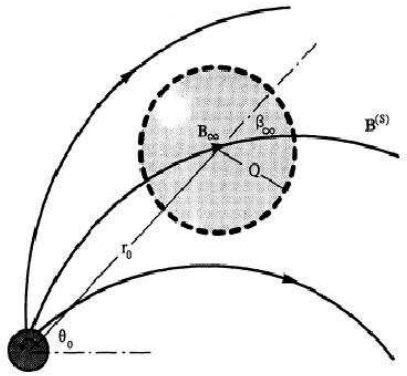

Figure 2.2: The figure from Yeh 1995 [6]. With the shaded area being the area of cross-section of the magnetic cloud. The bold lines being the spiral interplanetary magnetic field lines. While the magnetic cloud is moving along the heliographic equitorial plane.

Also the cloud's cross-sectional radius, denoted by $a(t)$. The assumption of varying cross-section is to account for the Lorentz self-force acting on the magnetic cloud. In terms of cylindrical coordinates (q,ϕ,z) aligned with the axis of the clouds, the velocity of the elemental magnetic cloud can be represented by

$$u_E(t; q, \phi, z) = u_0 + (1_q V + 1_\phi \Omega a)\frac{q}{a} \tag{2.4}$$

Hence, $u_0(t)$ denotes the translational velocity and V(t) denotes the expansional speed of the magnetic cloud, and $\Omega(t)$ denotes the angular speed at which the magnetic cloud is rotating about its axis. The ratio q/a remains invariant with time so that the periphery of the cross-section remains circular [6]. The magnetic field inside the cloud is entirely due to the internal currents that flow inside the cloud. The external currents which sustain the inter-planetary magnetic field, is canceled out because of the polarization current, induced on the interface that separates the magnetic cloud from the solar wind.

A simple current distribution is taken to define the permissible fields inside the magnetic cloud [13]:

$$B_E(t; q, \phi, z) = 1_z B_0\Big(1 - \frac{q^2}{a^2}\Big)^{1/2} + 1_\phi \frac{1}{2}\mu J_0 q,$$

produced by the current distribution:

$$J_E(t;q,\phi,z) = 1_z J_0 + 1_\phi \frac{\mu^{-1}B_0}{a}\frac{q/a}{\Big(1-q^2/a^2\Big)^{1/2}}$$

Each of these mass elements is subject to both Lorentz force of the magnetic field and the gradient force of gas pressure in addition to the gravitational force of the sun. Hence, the magnetic force density of the magnetic cloud:

$$J_E \times B_E = 1_q\Big(\frac{\mu^{-1}B_0^2}{a} - \frac{1}{2}\mu J_0^2 a\Big) \tag{2.5}$$

The expansional motion is driven by the force-density in the direction from the axis to the periphery. Hence, the equation of expansional motion is thus:

$$\rho_0\frac{d}{dt}V = \frac{\mu^{-1}B_0^2}{a} - \frac{1}{2}\mu J_0^2 a + 2\frac{p_0-p_\infty}{a} - 2\frac{\rho_\infty u_\infty^2 + \mu^{-1}B_\infty^2}{a} \tag{2.6}$$

Of which the self-induced Lorentz force resulting from self-interaction of the internal current is a part, another part is the gradient force resulting from the difference in internal (p_0) and external pressures (p_∞). There is also a contribution from the dynamic and magnetic pressures of the solar wind amplified from the interaction between the magnetic cloud and the surrounding solar wind(ρ_∞, u_∞ and B_∞ are the plasma density, velocity and magnetic field respectively associated with the solar wind).
If the gas pressure if completely ignored, the magnetic force in the fluxrope of the dynamical model will be zero when the ratio $\mu J_0 a/B_0$ is equal to $\pm 2^{1/2}$ (for left or right handed helicity). The required constraint in the case of force-free equilibrium gives us the situation where $\mu J_0 a/B_0$ equal to ± 2.405 (the first zero of the zeroth-order Bessel function), which in turn gives us:

$$B_E(q) = 1_z B_0 \jmath_0\Big(\ 2.405\frac{q}{a}\Big) + 1_\phi \frac{1}{2.405}\mu J_0 a \jmath_1\Big(2.405\frac{q}{a}\Big)$$

with the current distributed as

$$J_E(q) = 1_z J_0 \jmath_0\Big(2.405\frac{q}{a}\Big) + 1_\phi 2.405\frac{\mu^{-1}B_0}{a}\jmath_1\Big(2.405\frac{q}{a}\Big)$$

So with the radial velocity proportional to q/Q, the equation of expansional motion takes the form

$$\rho_0\frac{d}{dt}V = \frac{2.405^2}{2}\frac{\mu^{-2}B_0}{a} - \frac{1}{2}\mu J_0^2 a \tag{2.7}$$

This is the primary equation that will be used in studying the evolution of the minor radii.

Chapter 3

Methods

The actual fitting is done on the minor radius of the CME, obtained from the mapping of minor radius from SECCHI and LASCO data, and fitting it to a 5^{th} order polynomial w.r.t. time. Upon differentiating the polynomial fit to the minor radius vs. time data, we obtain the expansional velocity of the fluxrope. The expansional acceleration is obtained, upon double differentiating the polynomial.

Equation 2.7 is the theoretical prediction for the expansional accelerations for a magnetic cloud (cross-section of a CME). Upon using this fact we see the variation of Yeh's equation and with that try to check whether the behavior of acceleration over different time intervals is in good accordance with the actual acceleration found by double differentiating the the polynomial found when it was fit to the data.

We use LASCO data from the events in group A of Subramanian and Vourlidas, 2007 [14]. To which we fit the polynomial, on the minor radius.

We also use SECCHI data, to fit the Graduated Cylinder Shell model (figure 3.1) [5] for successive time stamps to obtain the evolution of the *major radius* of CME as a function of time and, hence simultaneously obtaining the *minor radius*. Based on the observed characteristics of CME velocity v(t) and acceleration profiles dv/dt(t) observed with SOHO/LASCO and SECCHI over the distance range of r = 2–30 R_0.

3.1 Analysis done on LASCO data

The data obtained from SOHO/LASCO data is an image of the projection of the event on the plane of the coronagraph, enabling us to just measure the parameters that are specific to that plane of view. LASCO, onboard the Solar and Heliospheric Observatory (SOHO), has two working coronagraphs observing the solar corona from $2.1R_0$ to about $32R_0$ with a cadence of about 40 minutes [16].

Two approaches were taken in this analysis:

i. In the first approach, the axial current is taken to be a constant, as mentioned

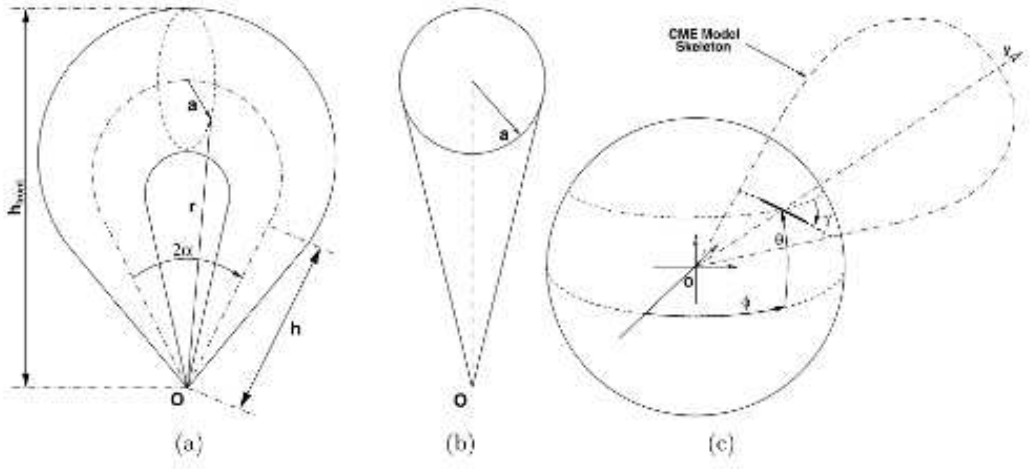

Figure 3.1: **Representations of the Graduated Cylindrical Shell (GCS) model**. (a) face-on and (b) edge-on . The dash-dotted line is the axis through the center of the shell. The solid line represents a planar cut through the cylindrical shell and the origin. O corresponds to the center of the Sun. (c) Positioning parameters. The loop represents the axis through the center of the shell, ϕ and θ are the longitude and latitude, respectively, and γ is the tilt angle around the axis of symmetry of the model[15].

in Subramanian and Vourlidas 2009 [5].

ii. In the second approach, the axial current varies inversely with respect to the major radius ($R^{-0.9}$), as mentioned in B. Kliem et al. 2010 [12].

3.1.1 For constant current:

When the axial current is assumed to constant, we use the equation of Subramanian and Vourlidas 2009 (eq. 2.2) [5], to compute the axial current. With $l_i = 0.5$ from Kliem and Torok 2006 [17], and also assuming the force-free scenario, in which all the other components like gravitational, magnetic and drag forces do not come into play. Upon computing the force by dividing the power generated by the velocity of CME, we then are able to arrive at the values for the axial current.

Upon dividing the current with the cross-sectional area of the CME, we get the current density. As the magnetic field is frozen in the CME, upon using the equation mentioned in DeVore 2000 [18]

$$\Phi = 1.4 B_0 a^2 \tag{3.1}$$

with ϕ, B_0 and a being the magnetic flux, axial magnetic field and the cross-sectional radius (minor radius) of the CME respectively. With the help of this equation the magnetic field associated with the CMEs were obtained. In Subramanian and Vourlidas 2009 [5], it was noted that the values of the magnetic flux was found to be a few times of 10^{21} Maxwell. Just concentrating on the proportionality, I took just 10^{21} Maxwell as the magnetic flux and obtained the various values of the associated magnetic fields at various time stamps.

With the help all the data, the values of accelerations were found, at various time intervals using the using equation 2.7. Then the acceleration found out by double differentiating w.r.t. time were overplotted on the the theoretical value and a correlation coefficient between the two were found, so as to ascertain the extent to which the two approaches have in common.

3.1.2 For variable current:

When the axial current is assumed to be variable, we use the equation 2.3, to compute the axial current. Just concentrating on the proportionalities, the axial current is computed:

$$AxialCurrent(I) = \frac{10^{18}}{R^{-n}} \tag{3.2}$$

The 10^{18} term in the equation 3.2 was chosen so as to match the exponent of the constant axial current obtained in the constant axial current section. The variable current is computed by varying the exponent of the major radius (n) from 0.5 to 1.2. With the value of n being 0.91 we get the maximum values for the correlation coefficient, hence the exponent value of 0.91 is retained for further analysis and hence, it is speculated that axial current flowing within the fluxropes varies with $R^{-0.91}$ as the CME propagates in space.

Upon dividing the current with the cross-sectional area of the CME, we get the current density. As the magnetic field is frozen in the CME, upon using the equation mentioned in DeVore 2000 [18]

$$\Phi = 1.4 B_0 a^2$$

with ϕ, B_0 and a being the magnetic flux, axial magnetic field and the cross-sectional radius (minor radius) of the CME. With the help of this equation the magnetic field associated with the CMEs were obtained. In Subramanian and Vourlidas 2009 [5], it was noted that the values of the magnetic flux was found to be few times of 10^{21} Maxwell. Just concentrating on the proportionality, I took just 10^{21} Maxwell as the magnetic flux and obtained the various values of the associated magnetic fields at various time stamps.
With the help all the data, the values of accelerations were found, at various time intervals using the using equation 2.7. Then the acceleration found out by double differentiating w.r.t. to time were overplotted on the the theoretical value and and a correlation coefficient between the two were found, so as to ascertain the extent to which the two approaches have in common.

3.2 Analysis done on SECCHI data

Upon using SECCHI data, we get the whole 3-D view of the event and the parameters we measure give us the real picture. The SECCHI instruments aboard the recently launched STEREO spacecraft enable for the first time the continuous tracking of coronal mass ejections (CMEs) from the Sun to 1 AU [19]. The coronagraphs

and heliospheric imagers part of the SECCHI investigation onboard STEREO are COR-1, COR-2, Heliospheric Imager 1, and Heliospheric Imager 2 (HI-1 and HI-2, respectively). Their fields of view are 2.13° ($4R_0$ with a $1.5R_0$ occulting disk), 8° ($15R_0$ with a $2R_0$ occulting disk), 20°, and 70°, respectively.
Also, the HIs are not pointed at the Sun but along the Sun Earth line and their fields of view are offset by an angle of 13.65° and 53.35° with respect to the Sun spacecraft line, respectively [20]. At the time of the ejections, STEREO was in its commissioning phase and STEREO-A was rolled by 22.4° from the solar north, which resulted in HI-1 and HI-2 imaging higher latitude regions than during the normal phase of the mission [20]. The spacecraft were separated by approximately 0.4° from Earth and were at a radial distance of $0.97AU$ from the Sun.

3.2.1 For variable current:

After downloading the FITS images from the SECCHI online database, those images were processed and converted from 0.5 level image to 1.0 image level using the software *SOLARSOFT IDL (SSWIDL)*. Then these images were grouped and further processed using the raytrace software suite mentioned in the SECCHI wiki page. Then with the help of a GUI the GRADUATED CYLINDER (GCS) MODEL is modeled on to these images.

The ray trace software suite is used to reproduce with a computer the image of a three-dimensional object as seen by an imaging device. The three-dimensional object can be either a solid object or a diffuse object. The Solar corona being a diffuse object: it is made of a plasma of electrons and particles of dust. These electrons and dusts scatter the light coming from the photosphere.
The main goal of the raytracing software is to reproduce by numerical simulation coronagraphic observations. These simulations are important to test different model and compare the simulated image with the true data. The software is also useful when designing new instruments to simulate the future observations [21] [22]).

The analysis is done, by using the same procedure mentioned in section 3.1.1 for the variable current subsection, on the data obtained from SECCHI.

Chapter 4

Results

Upon studying the evolution of the minor radius of the CME, a decent correlation is found between the theoretical and actual data, which in turn gives some credibility to prediction, that the axial current of the CME varies inversely as the major radius of the CME.

In the present study, we use the Graduated Cylindrical Shell (GCS) model of Thernisien, Howard, and Vourlidas (2006) (as shown in figure 4.12) to fit CME events observed by the SECCHI/COR2 A and B instruments.

Upon overplotting the LASCO data with a 5^{th} order polynomial, we check whether if a good fit is obtained on the data. After a decent fit is obtained for the data, we differentiate the polynomial twice w.r.t. time to obtain the acceleration by which the radial expansion of the CME takes place.
The analysis is divided into two sections:

i. We first take up the evolution of minor radius of the CME using LASCO data.

ii. We first take up the evolution of minor radius of the CME using SECCHI data.

4.1 Analysis done on LASCO data

The analysis in this section is further is divided in two parts. Depending on the variation of the axial current flowing within the fluxropes we try to ascertain that of the two; which is far more robust approach at looking at the rate at which the minor radius of the CME propogates, namely:

i. the axial current is taken to be a constant, as mentioned in Subramanian and Vourlidas 2009 [5].

ii. the axial current varies inversely with respect to the major radius ($R^{-0.9}$), as mentioned in B. Kliem et al. 2010 [12].

4.1.1 Analysis done on LASCO data, by assuming constant current.

Figure 4.1 - figure 4.4 show the plots for the various events, described below:

i. Plot for the minor radius vs. time. Also the 5^{th} order polynomial overplotted on it, and the correlation coefficient is mentioned between the two.

ii. Plot of the acceleration (dv/dt) vs time. The acceleration is obtained by double differentiating the polynomial w.r.t. time(denoted by the continuous line). The acceleration obtained by the Lorentz self-force is overplotted (denoted by the dashed line) and the coefficient of correlation is mentioned.

The table shown below (Table 4.1) gives us the dates of the event on the left hand side and on the right hand side are the correlation coefficients between the approaches of getting to the acceleration of the evolution of the minor radius of the CME, based on the assumption of constant axial current. As it is evident from the table that the there are a few events which show pretty good matches for the two approaches for calculating the accelerations, but it is not proof enough so as to obtain a clear picture from this data set.

4.1.2 Analysis done on LASCO data, by assuming variable current.

Figure 4.5 - Figure 4.8 show the plots for the various events, described below:

i. Plot for the minor radius vs. time. Also the 5^{th} order polynomial overplotted on it, and the correlation coefficient is mentioned between the two.

ii. Plot of the acceleration (dv/dt) vs time. The acceleration is obtained by double differentiating the polynomial w.r.t. time (denoted by the continuous line). The acceleration obtained by the Lorentz self-force is overplotted (denoted by the dashed line) and the coefficient of correlation is mentioned.

The table shown below (Table 4.2) gives us the dates of the event on the left hand side and on the right hand side are the correlation coefficients between the approaches of getting to the acceleration of the evolution of the minor radius of the CME, based on the assumption of variable axial current (varies inversely as $R^{0.9}$). As it is evident from the table that the two distinct groups in the table. One which shows negative values of the correlation coefficients, the other group shows high positive value, which implies that the variable axial current model takes well to the data.

The actual data in most cases shows a good correlation with the theoretical predictions. Implying that there the axial current within the fluxropes of the CME does decay at a rate some what inversely propotional to the major radius of the CME (R) as it moves out from the solar corona and into the interplanetary space, so as to conserve helicity.

Date[yy/mm/dd]	Fit of data
00/06/06	-0.48
00/08/02	0.12
00/08/03	**0.55**
00/11/17	-0.59
01/01/07	**0.71**
01/01/19	**0.52**
01/02/09	0.33
01/03/01	**0.57**
98/02/04	0.29
99/07/02	**0.89**
99/08/02	0.44
00/03/22	-0.68
00/05/05	-0.85
00/05/29	-0.75
00/10/26	-0.76
00/11/17	0.28
01/03/23	-0.68
97/11/01	-0.64
98/02/24	0.29
98/05/07	-0.70

Table 4.1: This table highlights the results obtained from the LASCO data. On the left hand column the date of the events are given. On the right hand side the correlation coefficient are mentioned that are obtained when we overplot the acceleration (by using the assumption of constant axial current) obtained by the equation 2.7.)

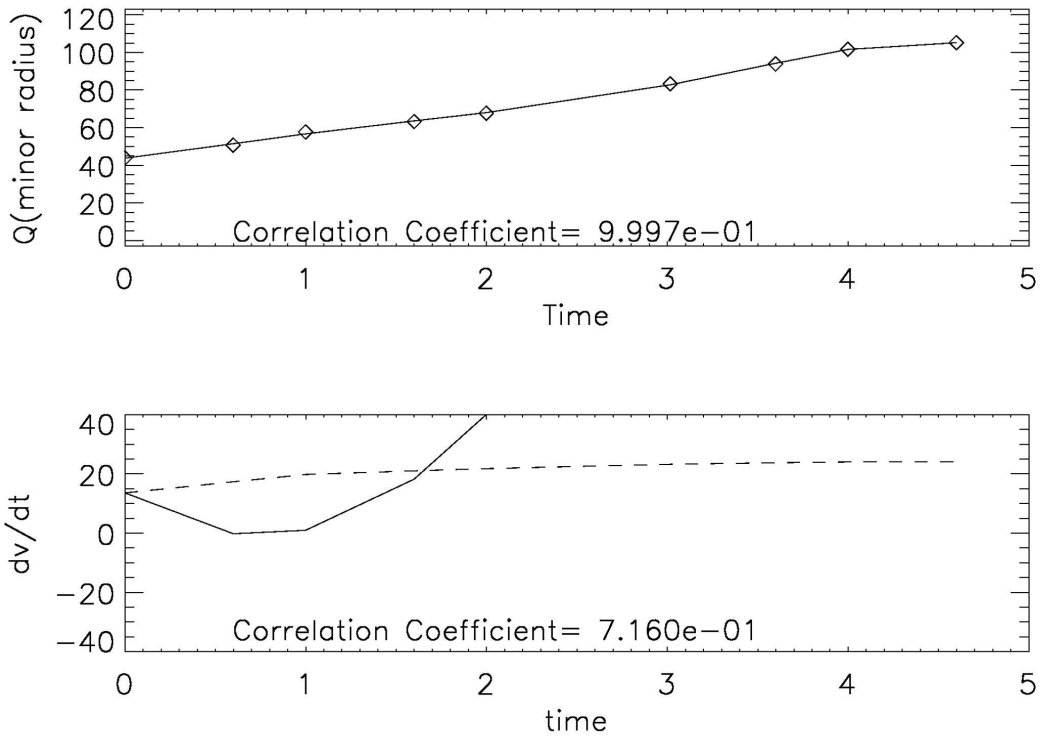

Figure 4.1: The plot shows two graphs. The first depicts the graph for the minor radius vs. time. Also the 5^{th} order polynomial overplotted on it, and the correlation coefficient is mentioned between the two. The second plot is of the acceleration (dv/dt) vs time. The acceleration is obtained by double differentiating the polynomial w.r.t. time (denoted by the continuous line). The acceleration obtained by the Lorentz self-force is overplotted (denoted by the dashed line) and the coefficient of correlation is mentioned (for the assumption of constant axial current). This is for the event on 7 Jan 2001.

4.2 Analysis done on SECCHI data

Upon using the raytrace software suite from the SECCHI wiki page we use the SECCHI data to call upon the GUI for the fitting of the wire cloud on the image of the coronagraph. Figure 4.12 shows the two FITS images which are view from the satellites COR-A and COR-B on which with the help of the GUI the wire frame model (in green) is fit. Table 4.3 shows the parameters upon which the Grdauated Cylinder Shell (GCS) model depends.

4.2.1 Analysis for the variable axial current

Further using the evolution of the Leading Edge (LE) of the CME with time we again fit a 5^{th} order polynomial to the minor radius w.r.t. time. Upon using the assumption of variable axial current of the fluxropes as mentioned in the section

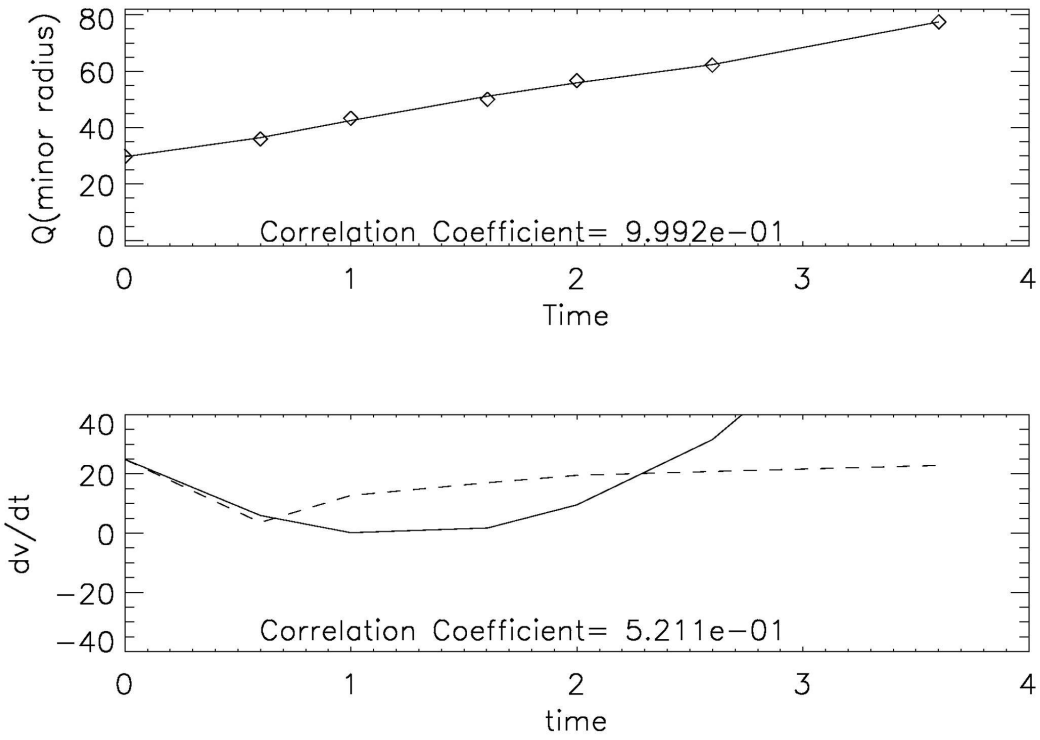

Figure 4.2: The description of this graph is same as figure 4.1. This is for the event on 19 Jan 2001.

4.1.2, so as to check whether the SECCHI data is in accordance with the theoretical predictions. Figure 4.9 - Figure 4.11 and Table 4.4 shows the parameters of the fitting done and the correlation coefficient between the two accelerations.

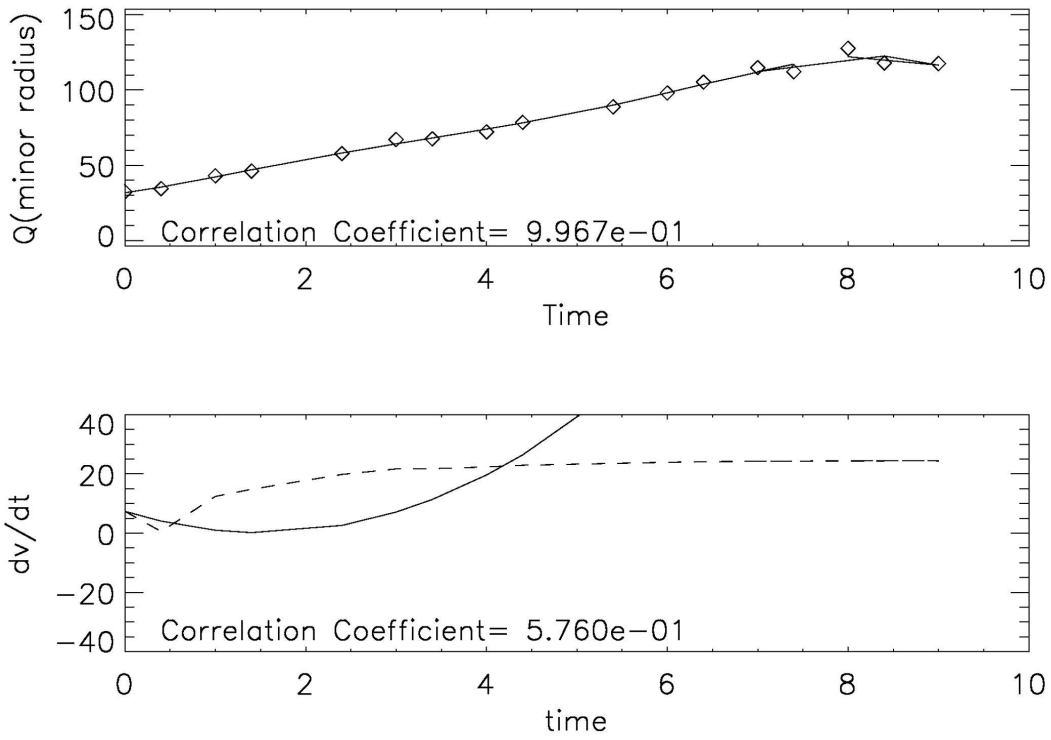

Figure 4.3: The description of this graph is same as figure 4.1. This is for the event on 1 Mar 2001.

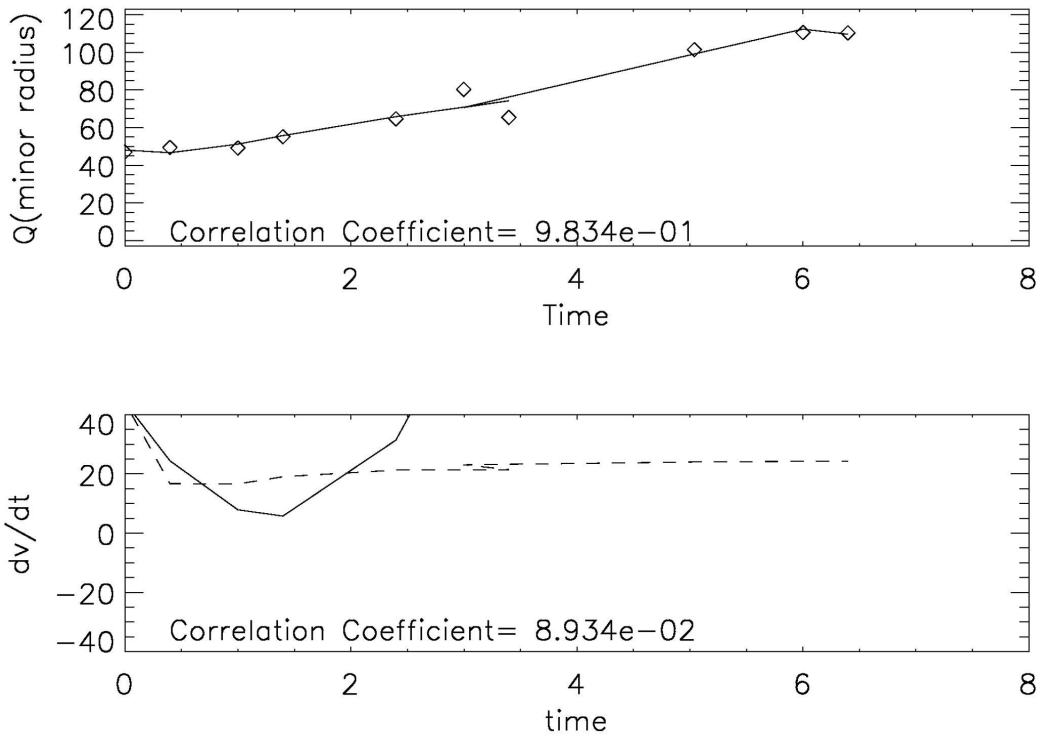

Figure 4.4: The description of this graph is same as figure 4.1. This is for the event on 2 Aug 1997.

Date[yy/mm/dd]	Fit of data
00/06/06	-0.534
00/08/02	-0.296
00/08/03	-0.342
00/11/17	-0.285
01/01/07	-0.356
01/01/19	-0.105
01/02/09	-0.353
01/03/01	-0.406
98/02/04	-0.244
99/07/02	-0.255
99/08/02	-0.443
00/03/22	**0.760**
00/05/05	**0.611**
00/05/29	**0.889**
00/10/26	**0.759**
00/11/17	**0.696**
01/03/23	**0.524**
97/11/01	**0.602**
98/02/24	**0.692**
98/05/07	**0.690**

Table 4.2: This table highlights the results obtained from the LASCO data. On the left hand column the date of the events are given. On the right hand side the correlation coefficient are mentioned that are obtained when we overplot the acceleration (by the using the assumption of variable axial current obtained by the equation 2.7).

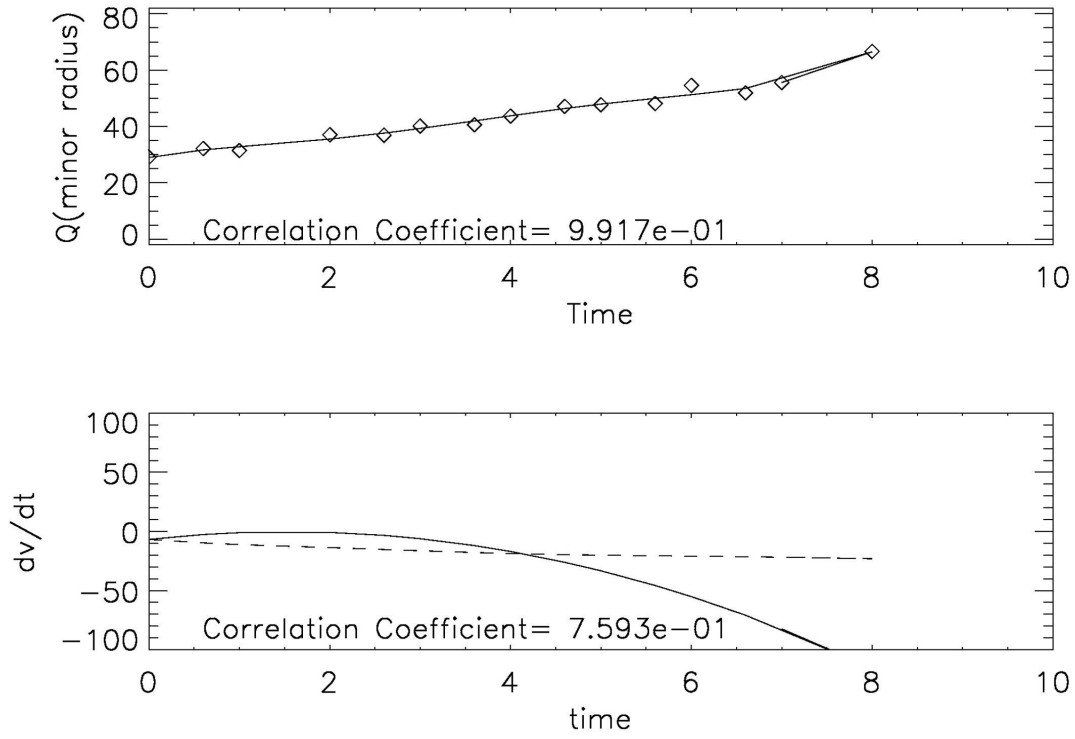

Figure 4.5: The plot shows two graphs. The first depicts the graph for the minor radius vs. time. Also the 5^{th} order polynomial overplotted on it, and the correlation coefficient is mentioned between the two. The second plot is of the acceleration (dv/dt) vs time. The acceleration is obtained by double differentiating the polynomial w.r.t. time (denoted by the continuous line). The acceleration obtained by the Lorentz self-force is overplotted (denoted by the dashed line) and the coefficient of correlation is mentioned (for the assumption of variable axial current). This is for the event on 26 Oct 2000.

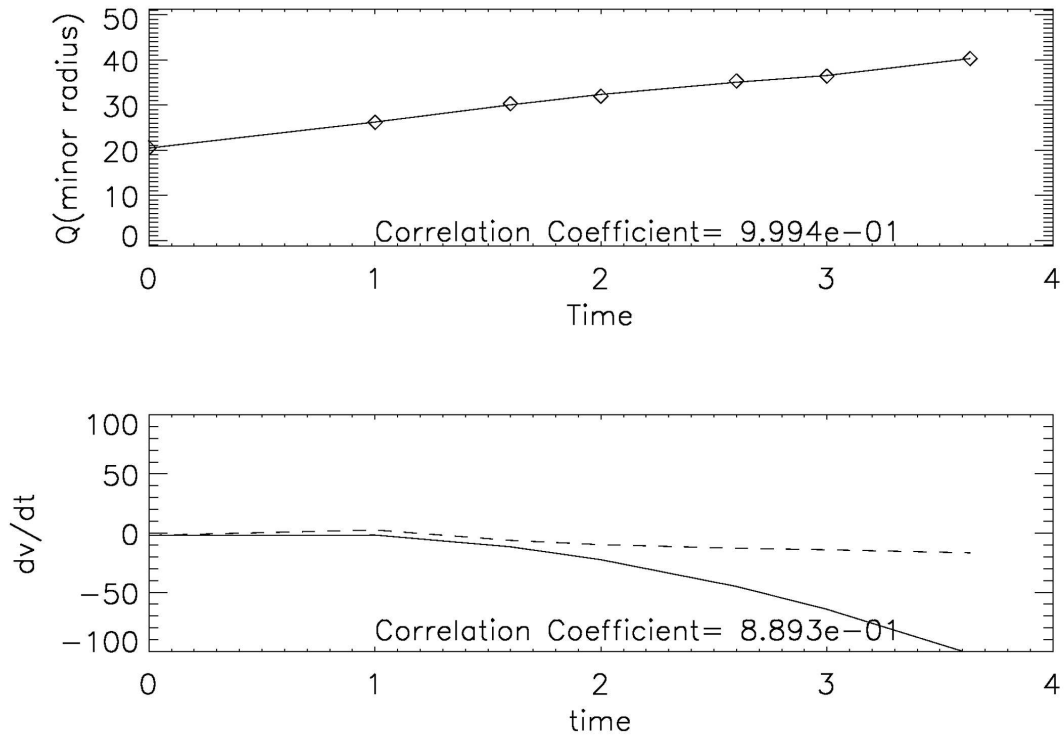

Figure 4.6: The description of this figure is same as 4.5. This is for the event on 29 May 2000.

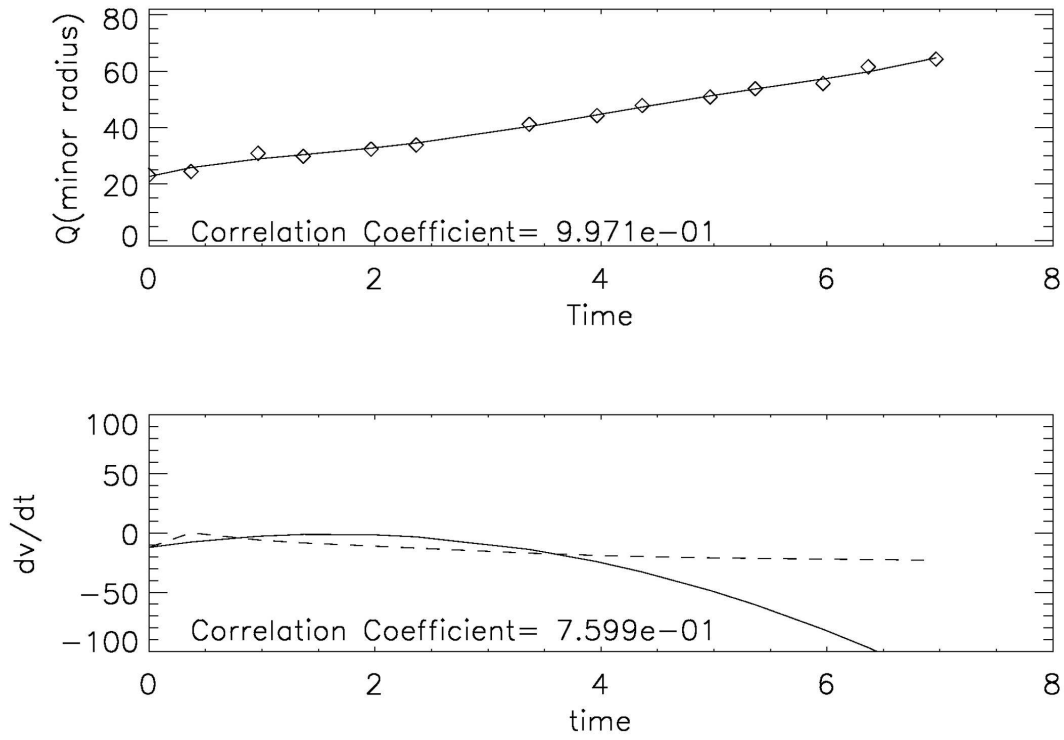

Figure 4.7: The description of this figure is same as 4.5. This is for the event on 22 Mar 2000.

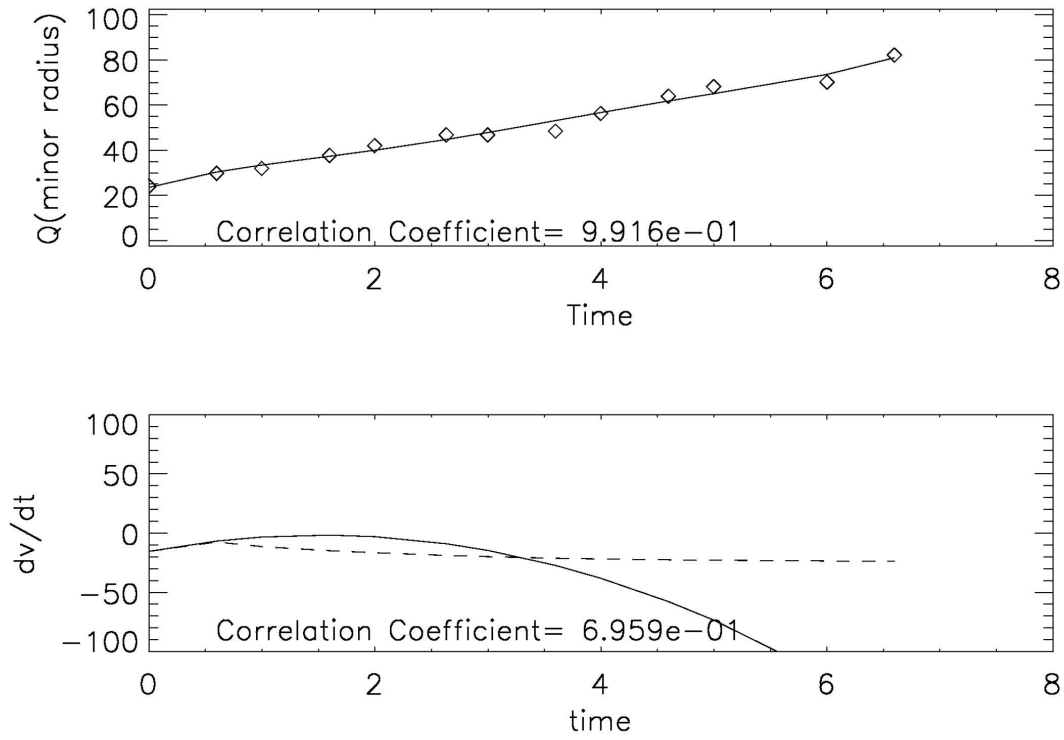

Figure 4.8: The description of this figure is same as 4.5. This is for the event on 17 Nov 2000.

Date	Time	θ	ϕ	γ	LE	κ	α
25/03/2008	19:22	199.004	-11.736	-44.162	4.49	0.203	21.2418
25/03/2008	19:52	199.004	-11.736	-44.162	7.50	0.203	21.2418
25/03/2008	20:22	199.004	-11.736	-44.162	10.07	0.203	21.2418
25/03/2008	20:52	199.004	-11.736	-44.162	12.28	0.203	21.2418
25/03/2008	21:22	199.004	-11.736	-44.162	15.00	0.203	21.2418
25/03/2008	21:52	199.004	-11.736	-44.162	16.92	0.203	21.2418
25/03/2008	22:22	199.004	-11.736	-44.162	18.32	0.203	21.2418
12/12/2008	08:22	73.78	7.26	87.20	4.92	0.10	18.16
12/12/2008	08:52	73.78	7.26	87.20	6.14	0.10	18.16
12/12/2008	09:22	73.78	7.26	87.20	6.64	0.10	18.16
12/12/2008	09:52	73.78	7.26	87.20	7.30	0.10	18.16
12/12/2008	10:22	73.78	7.26	87.20	7.64	0.10	18.16
12/12/2008	10:52	73.78	7.26	87.20	8.42	0.10	18.16
12/12/2008	11:22	73.78	7.26	87.20	9.82	0.10	18.16
12/12/2008	11:52	73.78	7.26	87.20	10.78	0.10	18.16
12/12/2008	12:22	73.78	7.26	87.20	11.85	0.10	18.16
12/12/2008	12:52	73.78	7.26	87.20	12.78	0.10	18.16
12/12/2008	13:22	73.78	7.26	87.20	14.07	0.10	18.16
12/12/2008	13:52	73.78	7.26	87.20	15.21	0.10	18.16
12/02/2008	17:22	243.72	-13.900	67.08	14.42	0.30	20.68
12/02/2008	18:22	243.72	-13.900	67.08	16.50	0.30	20.68
12/02/2008	18:52	243.72	-13.900	67.08	17.21	0.30	20.68
12/02/2008	19:22	243.72	-13.900	67.08	20.07	0.30	20.68
12/02/2008	19:52	243.72	-13.900	67.08	20.64	0.30	20.68
12/02/2008	20:22	243.72	-13.900	67.08	21.84	0.30	20.68
13/02/2008	16:22	351.05	17.88	-68.75	11.28	0.31	6.98
13/02/2008	16:52	351.05	17.88	-68.75	11.78	0.31	6.98
13/02/2008	17:22	351.05	17.88	-68.75	12.42	0.31	6.98
13/02/2008	17:52	351.05	17.88	-68.75	13.24	0.31	6.98
13/02/2008	18:22	351.05	17.88	-68.75	13.57	0.31	6.98
13/02/2008	18:52	351.05	17.88	-68.75	13.92	0.31	6.98
13/02/2008	19:22	351.05	17.88	-68.75	14.57	0.31	6.98
13/02/2008	19:52	351.05	17.88	-68.75	15.01	0.31	6.98
13/02/2008	20:22	351.05	17.88	-68.75	15.78	0.31	6.98
13/02/2008	20:52	351.05	17.88	-68.75	16.00	0.31	6.98
13/02/2008	22:22	351.05	17.88	-68.75	17.42	0.31	6.98
13/02/2008	23:22	351.05	17.88	-68.75	18.85	0.31	6.98
13/02/2008	23:52	351.05	17.88	-68.75	19.35	0.31	6.98
13/02/2008	00:22	351.05	17.88	-68.75	20.01	0.31	6.98

Table 4.3: This table shows the various parameters on which the GCS model depends. Namely, the Carrington Latitude, the Carrington Longitude, the tilt angle around the axis, the height of the Leading edge of the CME in solar radii, the aspect ratio and the half-angle between the legs respectively.

Date[yy/mm/dd]	Fit of data to prediction
08/03/25	**0.663**
08/02/13	**0.535**
08/02/12	0.113
08/12/12	**0.618**

Table 4.4: This table depicts the date of the event on the left. On the right the correlation coefficients are mentioned between the two accelerations, the first obtained by the double differentiating the polynomial fit on the data w.r.t. time and the other obtained (using the assumption of variable axial currents) by using equation 2.7

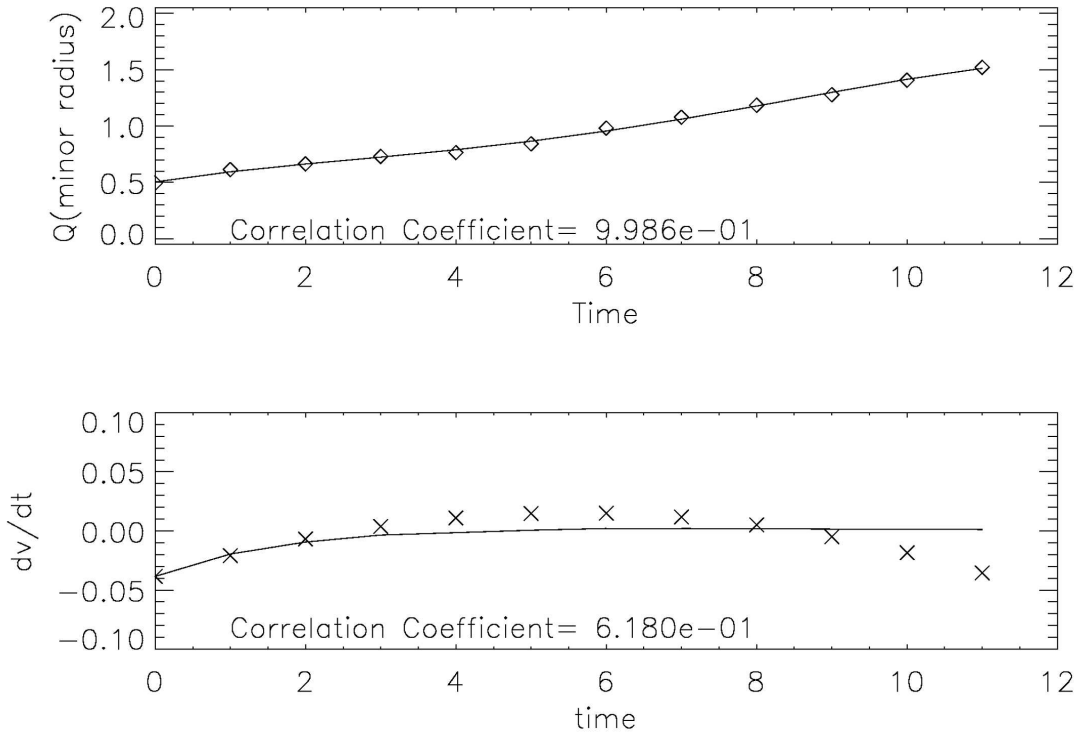

Figure 4.9: The plot shows two graphs. The first depicts the graph for the minor radius vs. time. Also the 5^{th} order polynomial overplotted on it, and the correlation coefficient is mentioned between the two. The second plot is of the acceleration (dv/dt) vs time. The acceleration is obtained by double differentiating the polynomial w.r.t. time (denoted by the continuous line). The acceleration obtained by the Lorentz self-force is overplotted (denoted by the dashed line) and the coefficient of correlation is mentioned (for the assumption of variable axial current). This is for the event on 12 Dec 2008.

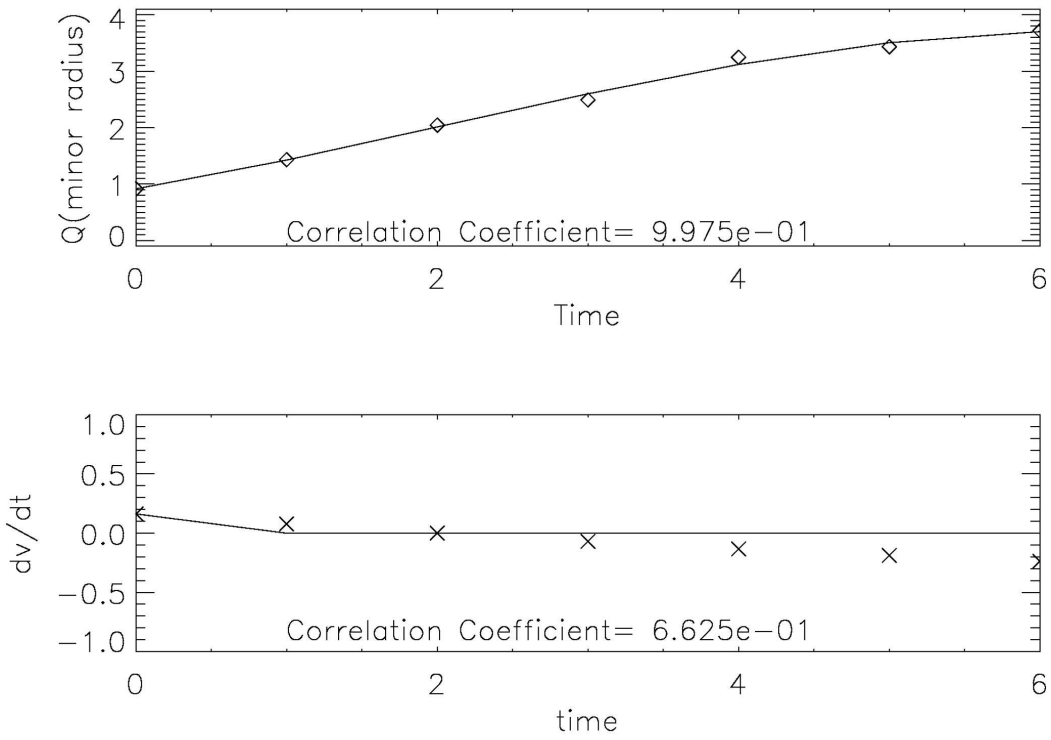

Figure 4.10: The description of this figure is same as figure 4.9. This is for the event on 25 Mar 2008.

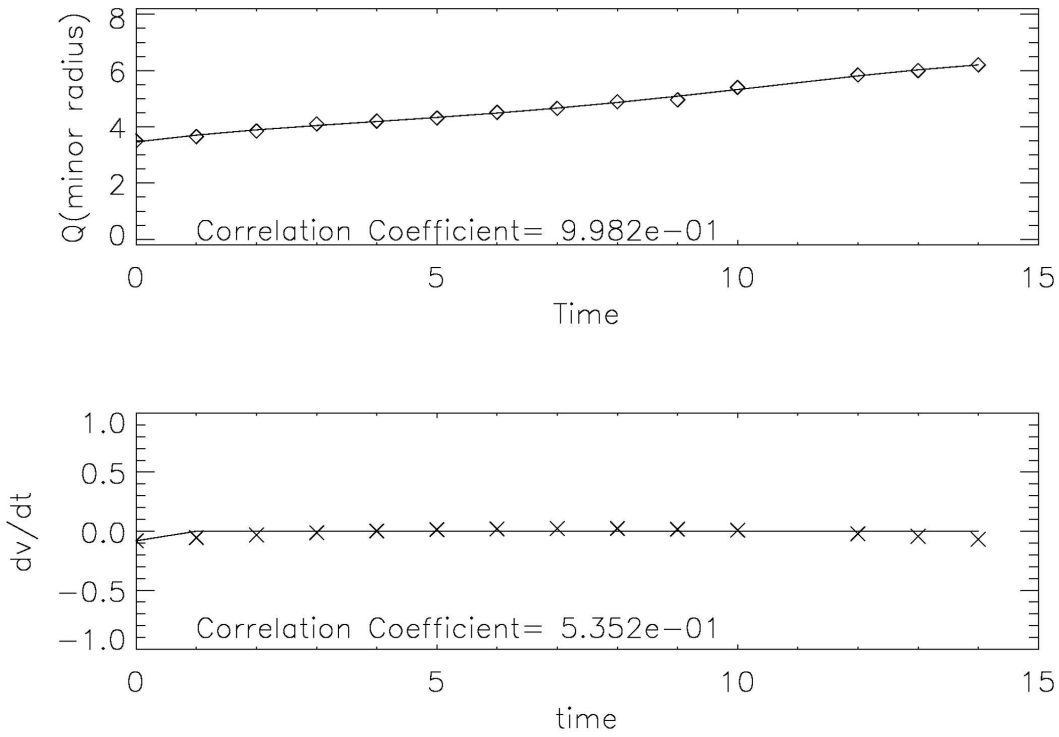

Figure 4.11: The description of this figure is same as 4.9. This is for the event on 13 Feb 2008.

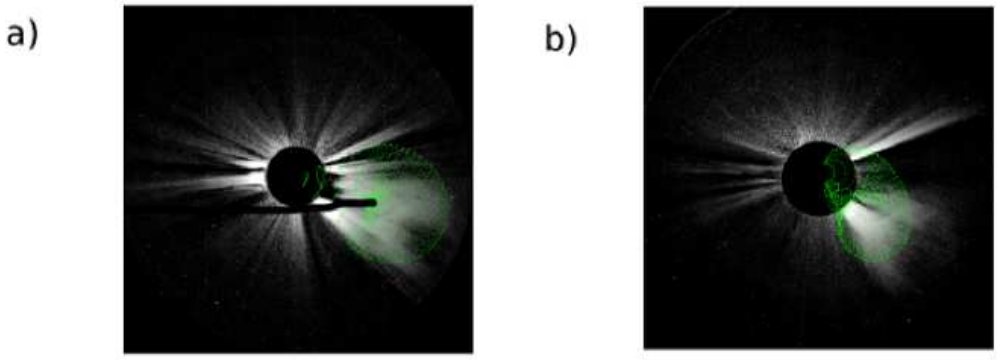

Figure 4.12: The figure depicts the wire frame model (GCS) modeled upon the FITS (Flexible Image Transport System) images, with help of the GUI from the ray trace software suite. a) Depicts the view from spacecraft COR-A. b) Depicts the view from spacecraft COR-B. The wireframe rendering gives a 3-D view, which provides the actual parameters for the event.

Chapter 5

Discussion

After analyzing the data from both the satellites (LASCO and SECCHI), various conclusions can be drawn, which do provide an insight on the nature of the expansion of the minor radius of the coronal mass ejections due to the Lorentz self-forces. Upon determining the acceleration by double differentiating the fitting polynomial wrt time. Then the acceleration of the CME is computed from equation 2.7 and the plotted together to see, how they match. Also with the help of the SECCHI data, the total surface area of the CME can be obtained which is instrumental in the determination of the drag forces acting on the CME.

5.1 For LASCO data

Upon checking the consistency of the rate of the expansion of the CME with the theoretical considerations of the Lorentz self-force, a considerable amount of evidence was obtained to support the hypothesis that to conserve helicity the axial current decays at a rate of approximately R^{-1}. Upon observing Table 4.2, there are a lot of events, which show a decent match with the theoretical values to the actual data. The matching for most being above 0.65. Also in the same table, there are same events that match poorly with the data. Hence, nothing concrete can be determined from the analysis and it can only be speculated that the axial current of the fluxrope might decay at the CME moves forward.

Upon observing the table 4.1, we find that a decent match are too few and in between, also while the rest of the data match poorly with the data, hence with better certainty we it can be speculated that the axial current does not remain constant as it CME moves outwards into interplanetary space.

5.2 For SECCHI data

Four events were observed with the help of the SECCHI data. As the LASCO data gave us the partial picture of what exactly happened (being just a 2-D projection in the plane of the image), SECCHI on the other hand gives us the full 3-D

picture of the event, and hence the parameters observed are real in terms of significance.
Upon observing the table 4.4, we find that there is a decent match between the two theoretical and actual data. As the number of events observed are here are very small, as compared to LASCO data, again we can't say for sure, but still can speculate that to conserve helicity the axial current of the fluxropes of the CME does vary at a rate proportional to R^{-1}.

References

[1] S. K. Anttichos, C. R. Devore, J. A. Klimchuk, A model for coronal mass ejections, ASTROPHYS J 485 (485).

[2] M. J. Aschwanden, Physics of the Solar Coronal, Praxis Publishing, 2009, Ch. Coronal Mass Ejections, pp. 703–737.

[3] J. Chen, Theory of prominence eruptions and propogations: Interplanetary consequences, J GEOPHYS RES 101 (1996) 27449–27519.

[4] A. Kumar, D. M. Rust, Interplanetary magnetic clouds, helicity conservation, and and current-core fluxropes, J GEOPHYS RES 101 (1996) 15667–15684.

[5] P. Subramanian, A. Vourlidas, Driving currents for fluxrope coronal mass ejections, ASTROPHYS J 693 (2010) 1219–1222.

[6] T. Yeh, A dynamical model of magnetic clouds, ASTROPHYS J 438 (1995) 975–984.

[7] M. Vandas, E. P. Romashets, Magnetic field in an elliptic fluxrope: A generalization of the lundquist ssolution, in: Solar Variablity: From Core to the outer frontiers, Vol. 506 of Proc. 10th European Solar Physics Meeting, 2002.

[8] S. Lundquist, Experimental investigation of magneto-hydrodynamic waves, PHYS REV 76 (1949) 1805–1809.

[9] A. Kumar, D. M. Rust, Helical magnetic fields in filaments, Sol Phys 155 (1994) 69.

[10] P. Demoulin, S. Dasso, Causes and consequences of magnetic cloud expansion, ASTRON ASTROPHYS 498 (2) (2009) 551–566.

[11] Y. Wang, J. Zhang, C. Shen, An analytical model probing the internal state of coronal mass ejections based on observations of their expansions and propagations, Solar and Stellar Astrophysics.

[12] B. Kliem, S. Rust, N. Seehafer, Helicity transport in a a simulated coronal mass ejection, in: A. Bonanno, E. de. Gouveia, A. Kosovichev (Eds.), Advances in Plasma Astrophysics, Vol. 274 of Proceedings IAU Symposium, 2011.

[13] T. Yeh, Hydromagnetic buoyancy force in the solar atmosphere, Sol Phys 95 (1985) 83–97.

[14] P. Subramanian, A. Vourlidas, Energetic of solar coronal mass ejections, ASTRON ASTROPHYS 467 (2007) 685–693.

[15] A. Thernisien, V. A, R. A. Howard, Forward modelling of coronal mass ejections using stereo/secchi data, Sol Phys 256 (2009) 111–130.

[16] G. E. Brueckner, R. A. Howard, M. J. Koomen, C. M. Korendyke, D. J. Michels, J. D. Moses, D. G. Socker, K. P. Dere, P. L. Lamy, A. Llebaraia, M. V. Bout, R. Schwenn, G. M. Simnett, D. K. Bedford, , C. J. Eyles, Sol Phys 162 (1995) 357.

[17] B. Kliem, T. Torok, Torous instabilty, PHYS REV LETT 96.

[18] C. R. Devore, Magnetic helicity generation by solar differential rotation, ASTROPHYS J 539.

[19] N. Lugaz, J. N. Hernandez-Charpak, I. I. Roussev, C. J. Davies, A. Vourlidas, J. A. Davies, Determining the azimuthal properties of coronal mass ejections from multi-spacecraft remote-sensing observations with stereo secchi, ASTROPHYS J 715.

[20] R. A. Howard, J. D. Moses, A. Vourlidas, J. S. Newmark, D. G. Socker, S. P. Plunkett, C. M. Korendyke, J. W. Cook, et al., Sun earth connection coronal and heliospheric investigation (secchi), SPACE SCI. REV. 136 (2008) 67–115.

[21] W. T. Thompson, Coordinate systems for solar image data, ASTRON ASTROPHYS 449 (2006) 791–803.

[22] M. R. Calabretta, E. W. Greisen, Representation of celestial coordiantes in fits, ASTRON ASTROPHYS 395 (2002) 1077–1122.

[23] P. J. Cargill, On the aerodynamic drag force acting on the interplanetary coronal mass ejections, Sol Phys 221 (2004) 135–149.

Appendix A

Surface Area Calculations

The dynamics of an CME is determined (equation 2.2) by (a) the outward or inward Lorentz force, (b) the inward gravitational force and (c) forces due to the interaction of the CME with the solar wind, referred to as the drag force(p cargill 2004). There are a lot difficulties in determining the drag forces as it is dependent on a number of independent factors. The drag force can be quantified in terms of [23]:

$$F_{drag} = \rho_e A C_D (V_i - V_e)|V_i - V_e|$$

where ρ_e is the solar wind density, A is the total surface area of the CME, V_i is the velocity of the CME and V_e is velocity of the solar wind. Hence, it is imperative to know the total surface area of the CME so that exact calculations can be made to determine the drag forces that act on the CME.

Upon observing the GCS model (referring to figure 3.1), a conclusion is made that the model is actually made up of three parts. One being the partial torus fitted on top of the legs with the major radius **r** and the minor radius **a**. The other two parts being the conical legs of the CME with radius as **a** and the height mentioned as h. By using the raytrace software, we are able to determine h_{ext} or the height of the leading edge of the CME in solar radii, the half angle between the legs α and κ: the aspect ratio (from table 4.3), which are vital for the calculations for the parameters such as h, a and r. This can be done by using the equations:

$$a = \kappa r$$

$$h = h_{ext}(1 - \kappa)/\tan(\frac{\pi}{4} + \frac{\alpha}{2})$$

Furthermore, we also come to conclude on observing the figure A.1 that:

$$r + a = h_{ext} \tag{A.1}$$

hence upon using the equation 1 in the paper of A. Thernisien et. al 2009 [15] , we get:

$$r = \frac{h_{ext}}{1 + \kappa}, a = \frac{\kappa h_{ext}}{1 + \kappa} \tag{A.2}$$

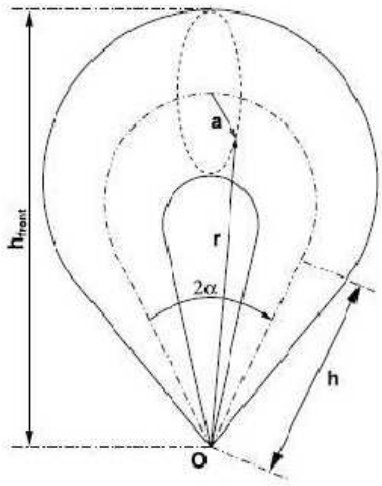

Figure A.1: **Representations of the face-on Graduated Cylindrical Shell (GCS) model**

Now, to calculate the total surface area we first need to calculate the surface area of the two cones.

$$S_{cones} = 2\pi a\sqrt{h^2 + a^2}$$

The surface area of the torus is:

$$S_{torous} = 2\pi a(\pi + 2\alpha)[r - h\sec(\alpha)]$$

Hence, the total surface area of the whole model can be calculated by summing up the surface area of the two cones and the torus:

$$S_{total} = 2 \times 2\pi a\sqrt{h^2 + a^2} + 2\pi a \times (\pi + 2\alpha)[r - h\sec(\alpha)] \tag{A.3}$$

Appendix B

Results obtained from the surface area calculations

Upon using equation A.3, we compute the total surface area of the CME and it is plotted against time, for the various events. Figure B.4 shows the plots of the total surface area with time, for the various events.

Upon observing the total surface area of the events and plotting them w.r.t time, we see a gradual increase in the surface area as time progresses. By studying the evolution of the total surface area, we are one step further in estimating the drag force acting on the CME as it propogates further in time. This information is vital as it actually gives us the complete surface area of the CME as compared to the LASCO data, which is just a projection of the CME on the plane of projection. The drag force on CME is not an easy quantity to determine as it depends on various parameters which keep changing with each event. By determining the total surface area of the CME, we at least have the information about one of the factors and which in its own is a huge step.

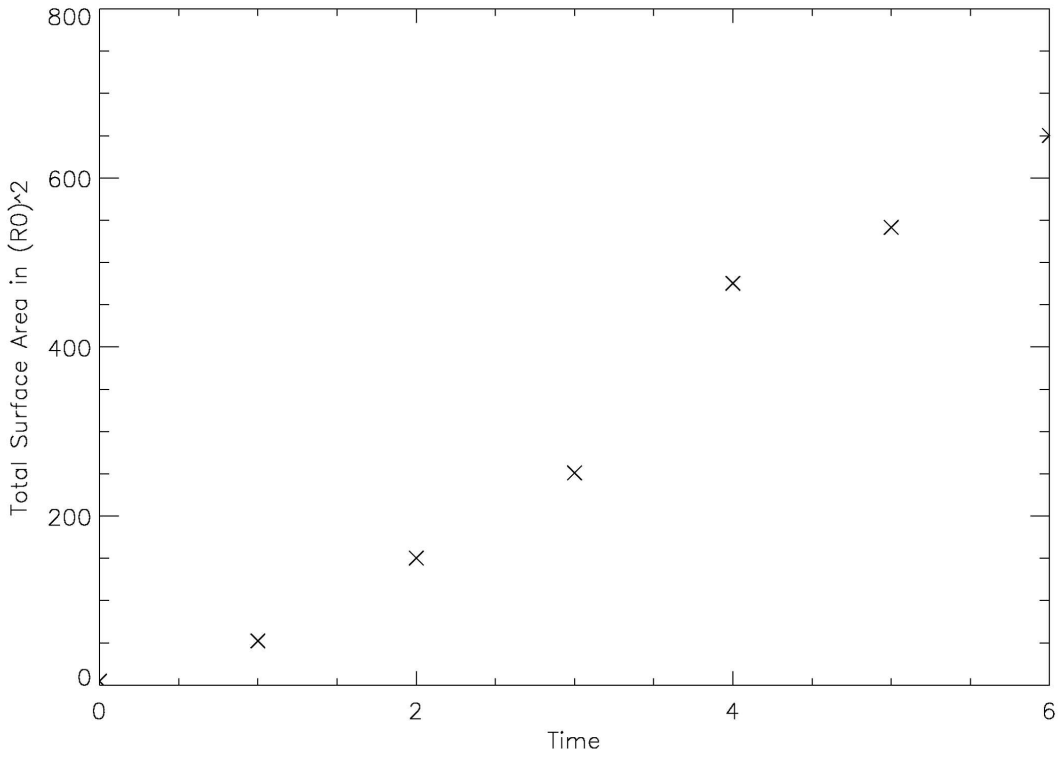

Figure B.1: This figure shows the plot of the total surface area of the CME with time. Depicts the plot for the event on 25 Mar 2008.

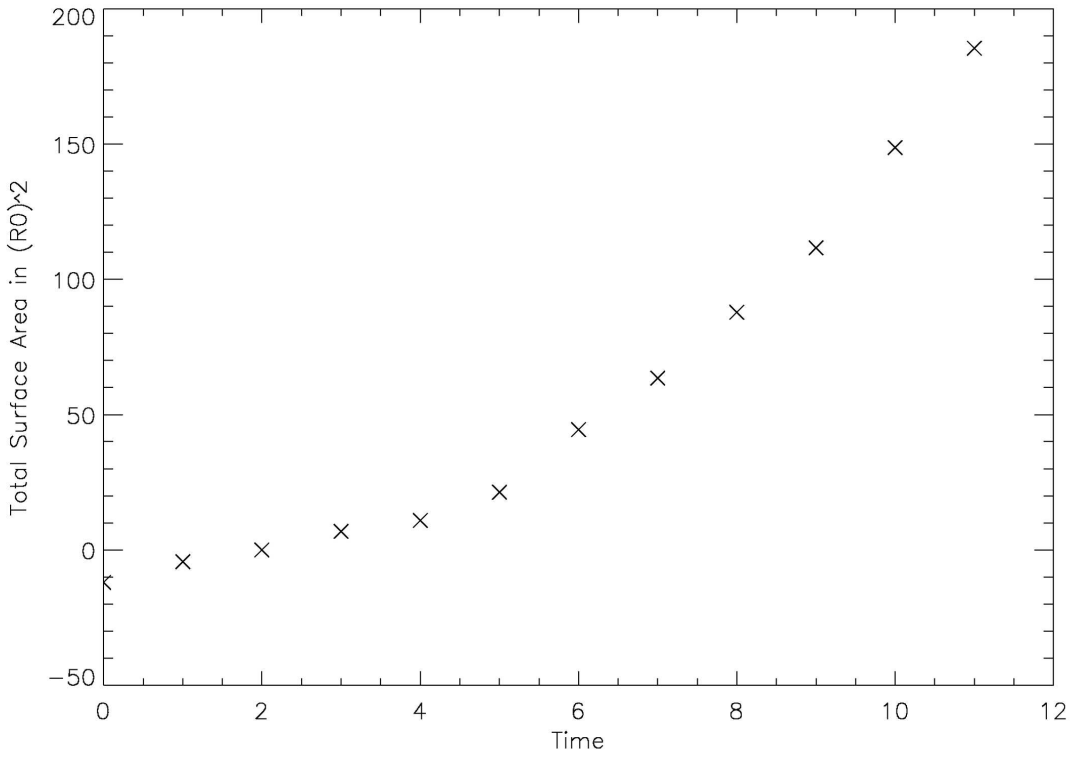

Figure B.2: This figure shows the plot of the total surface area of the CME with time. Depicts the plot for the event on 12 Dec 2008.

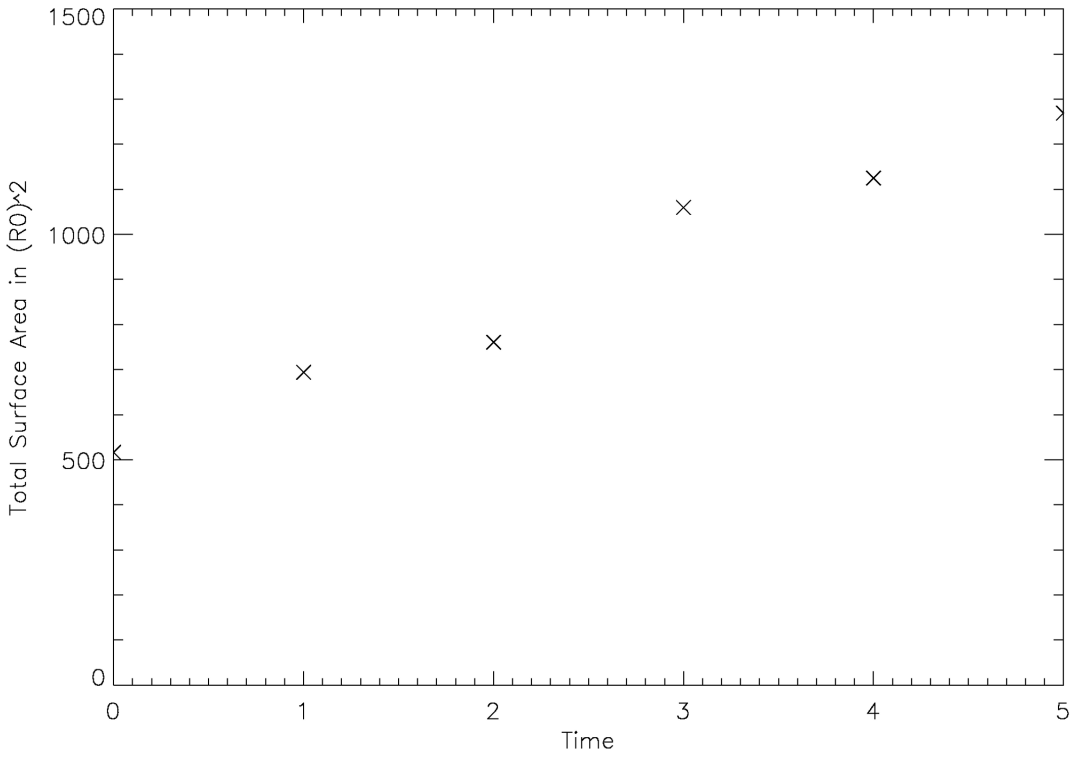

Figure B.3: This figure shows the plot of the total surface area of the CME with time. Depicts the plot for the event on 12 Feb 2008.

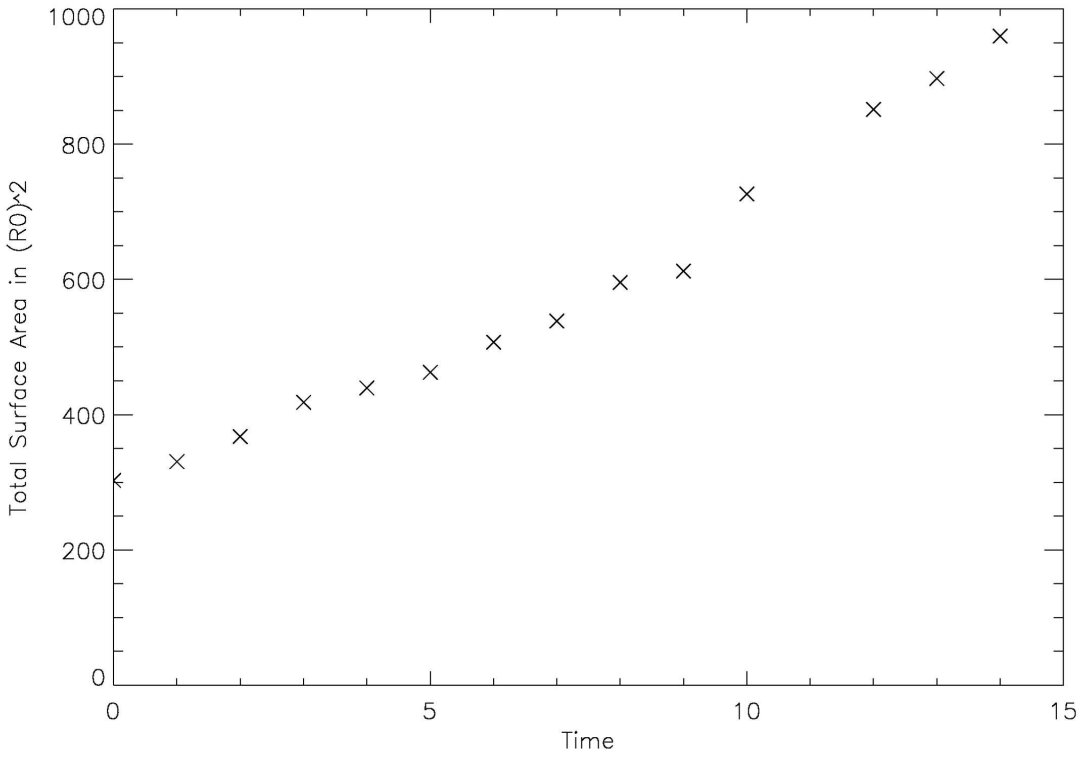

Figure B.4: This figure shows the plot of the total surface area of the CME with time. Depicts the plot for the event on 13 Feb 2008.